Supplementary information

Evidence of underlying structural similarities of amorphous materials

Akihiko Hirata[1,2,3,4,5*], Kengo Nishio[6,4*], Masayuki Okugawa[7,8], Ryusuke Nakamura[9]

1. Department of Applied Mathematics / Department of Materials Science, Waseda University, Shinjuku, Tokyo, 169-8555, Japan

2. Kagami Memorial Research Institute for Materials Science and Technology, Waseda University, Shinjuku, Tokyo, 169-0051, Japan

3. WPI Advanced Institute for Materials Research, Tohoku University, Sendai, Miyagi 980-8577, Japan

4. Mathematics for Advanced Materials-OIL, AIST, Sendai, Miyagi 980-8577, Japan

5. Center for Basic Research on Materials, National Institute for Materials Science, Tsukuba, 305-0047, Japan

6. Materials DX Research Center, National Institute of Advanced Industrial Science and Technology (AIST), 1-1-1 Umezono, Tsukuba, Ibaraki 305-8568, Japan

7. Division of Materials and Manufacturing Science, Graduate School of Engineering, Osaka University, 2-1 Yamadaoka, Suita, Osaka 565-0871, Japan

8. Anisotropic Design & Additive Manufacturing Research Center, Osaka University, 2-1 Yamadaoka, Suita, Osaka 565-0871, Japan

9.Department of Materials Science, School of Engineering, The University of Shiga Prefecture, Hassaka-cho 2500, Hikone 522-8533, Japan

Supplementary Table1, Supplementary Figure 1 – Supplementary Figure 15

Supplementary Table

Supplementary Table 1 Parameter values for the WCA-MBKS potential:

$$\varphi_{XY}^{WCA-MBKS} = \varphi_{XY}^{WCA} + \varphi_{XY}^{MBKS}$$

$$\varphi_{XY}^{WCA}(r) = \begin{cases} \varphi_{XY}^{LJ}(r) - \varphi_{XY}^{LJ}\left(2^{1/6}\sigma_{XY}\right), & r < 2^{1/6}\sigma_{XY} \\ 0, & r \geq 2^{1/6}\sigma_{XY} \end{cases}$$

$$\varphi_{XY}^{LJ}(r) = 4\varepsilon_{XY}\left(\left(\frac{\sigma_{XY}}{r}\right)^{12} - \left(\frac{\sigma_{XY}}{r}\right)^{6}\right)$$

$$\varphi_{XY}^{MBKS} = \varphi_{XY}^{Morse} + \varphi_{XY}^{BKS}$$

$$\varphi_{XY}^{Morse}(r) = \alpha_{XY}\left(1 - e^{-\beta_{XY}(r-\gamma_{XY})}\right)^2 - \alpha_{XY}$$

$$= \alpha_{XY}\left(e^{-2\beta_{XY}(r-\gamma_{XY})} - 2e^{-\beta_{XY}(r-\gamma_{XY})}\right)$$

$$\varphi_{XY}^{BKS}(r) = K\frac{q_X q_Y}{r} + A_{XY}\exp(-r/B_{XY}) - \frac{C_{XY}}{r^6}$$

Here, X and Y each represent an element, either Hf or O. $K = e^2/4\pi\varepsilon_0$, where e is the elemental charge and ε_0 is the vacuum permittivity. The parameter values for the MBKS term are identical with those reported in the literature [J. P. Trinastic, R. Hamdan, Y. Wu, L. Zhang, Hai-Ping Cheng, J. Chem. Phys. 139, 154506 (2013)].

XY	ε (eV)	σ (Å)	α (eV)	β (Å^{-1})	γ (Å)	A(eV)	B(Å^{-1})	C(eV Å^6)
OO	10	1.3	0	-	-	1388.77	0.3623	175.00
HfO	10	0.9	0.3474	1.6230	2.0480	12372.16	0.2286	81.36
HfHf	0	-	0	-	-	0	-	0

$q_{Hf} = 2.4$

$q_O = -1.2$

Supplementary figures

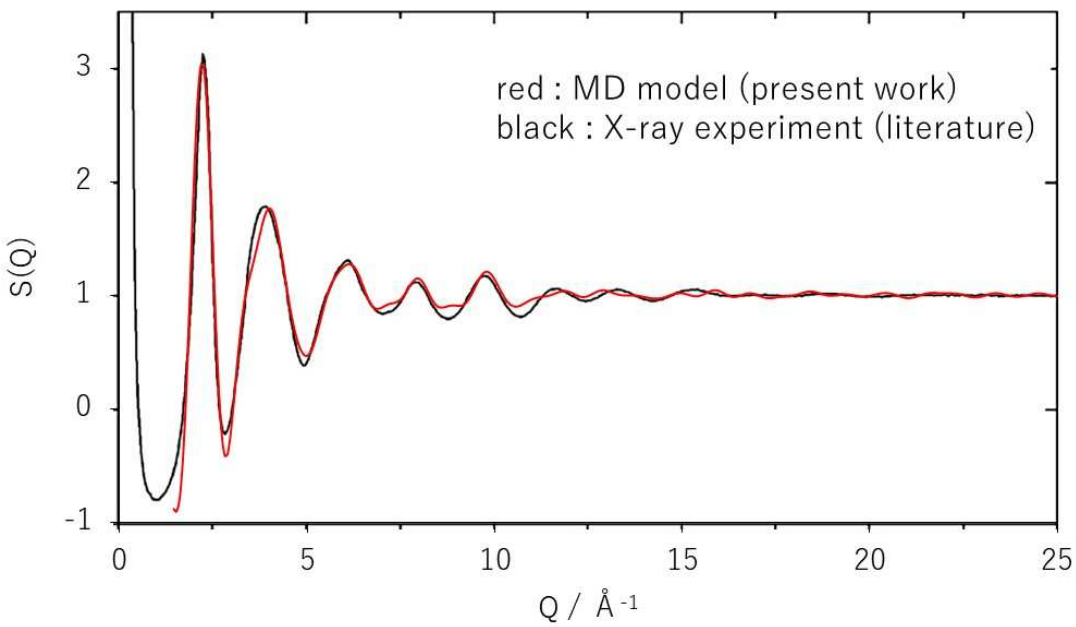

Supplementary Fig. 1　Comparison between the X-ray structure factor calculated from the *ab initio* MD model of amorphous HfO_2 and the experimental X-ray structure factor reported in the literature [L. C. Gallington *et al.*, Materials 10, 1290 (2017)]. The overall agreement between the two profiles supports the validity of the simulated atomic configuration.

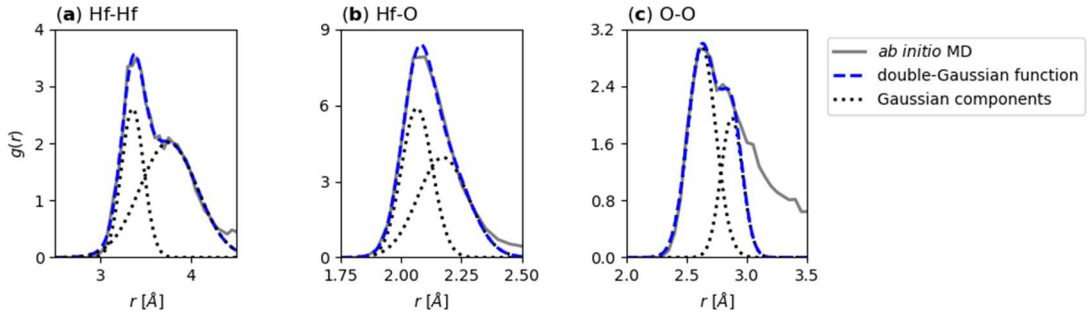

Supplementary Fig. 2 First peaks of the partial pair distribution functions, g(r)s, computed using *ab initio* MD simulations. Our results are compared with those reported by L. C. Gallington *et al.* [L. C. Gallington *et al.*, Materials 10, 1290 (2017)] (a) Hf-Hf pairs: L. C. Gallington *et al.* experimentally showed that the peak in the pair distribution function corresponding to Hf-Hf bonds is split, with the subpeak positions at 3.38 and 3.89 Å. A clear split is not observed in our g(r) for Hf-Hf pairs. However, our g(r) can be well fitted with a double-Gaussian function composed of two Gaussians centered at 3.35 and 3.75 Å, consistent with the experimental results. (b) Hf-O pairs: the peak is well fitted with a double-Gaussian function. The double-Gaussian function yields the peak position 2.07 Å. This value is consistent with the experimental result, 2.13 Å, by L. C. Gallington *et al.* Using a cutoff distance of 2.65 Å, corresponding to the minimum in the valley between the first and second peaks, the average number of O atoms around an Hf atom is determined to be 6.6. This value is consistent with the experimental result, 6.8, by L. C. Gallington *et al*. (c) O-O pairs: a double-Gaussian function was used to determine the peak position, which was found to be 2.63 Å.

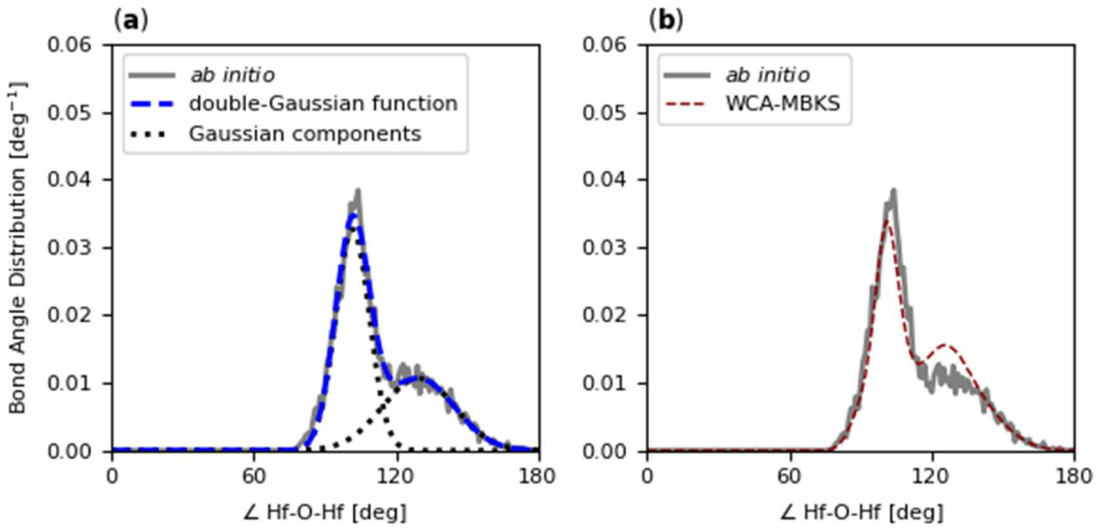

Supplementary Fig. 3 Distribution of Hf-O-Hf bond angles in amorphous HfO_2. (a) Bond angle distribution obtained from *ab initio* MD simulations. The result is well fitted with a double-Gaussian function composed of two Gaussians centered at 102° and 129°. This is consistent with the classical molecular dynamics results by L. C. Gallington *et al.,* who reported peaks at 102° and 135°. (b) Comparison of the bond angle distribution obtained from *ab initio* and classical MD simulations using the WCA-MBKS potential. Both models were generated using a cooling rate of 1.0×10^{15} K s^{-1}. Overall, the two results are in good agreement.

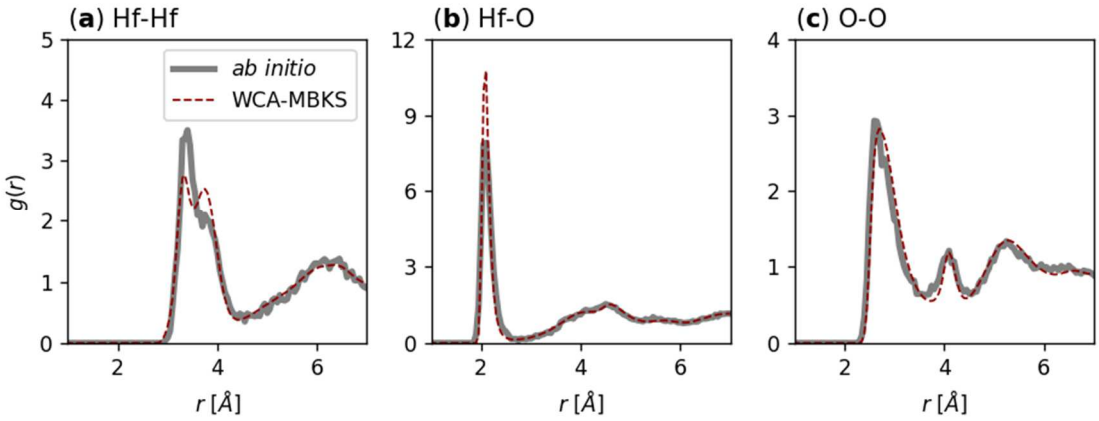

Supplementary Fig. 4 Comparison of the partial pair distribution functions, g(r)s, obtained from *ab initio* and classical MD simulations using the WCA-MBKS potential for (a) Hf-Hf pairs, (b) Hf-O pairs, and (c) O-O pairs. Both models were generated using a cooling rate of 1.0×10^{15} K s^{-1}. Overall, the two results are in good agreement. However, a clear splitting is observed in the first peak in the Hf-Hf pair distribution function from the WCA-MBKS potential, whereas it is not evident in the *ab initio* result.

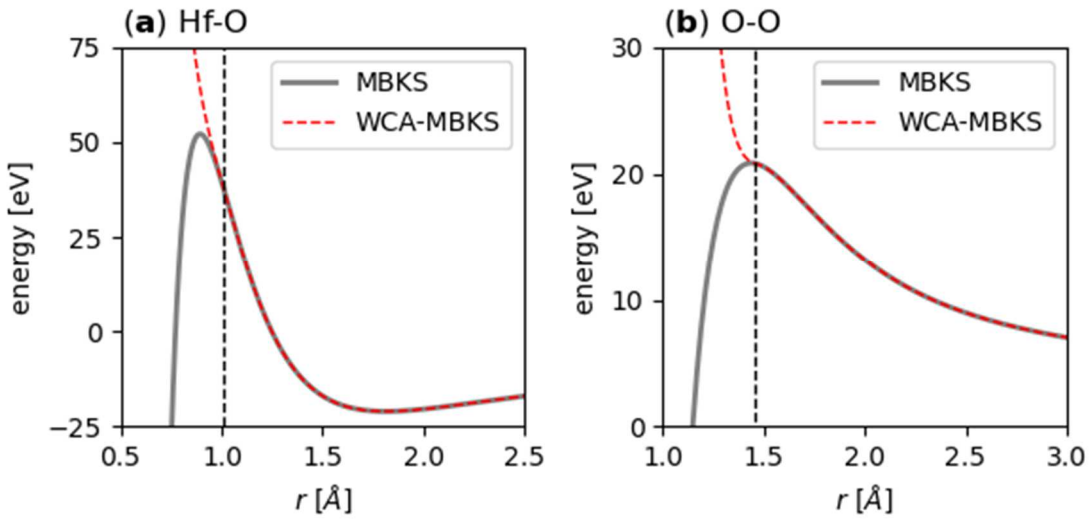

Supplementary Fig. 5　Comparison of the MBKS and WCA-MBKS potentials for (a) the Hf-O pair and (b) the O-O pair. In each graph, the vertical dashed line indicates the distance $2^{1/6}\sigma_{XY}$, below which the WCA term is nonzero. Beyond this point, the WCA-MBKS potential is equal to the MBKS potential. The WCA term eliminates the unphysical attractive interaction at short distances which may occur at high temperatures in the MBKS potential, without changing the energy relevant at low temperatures.

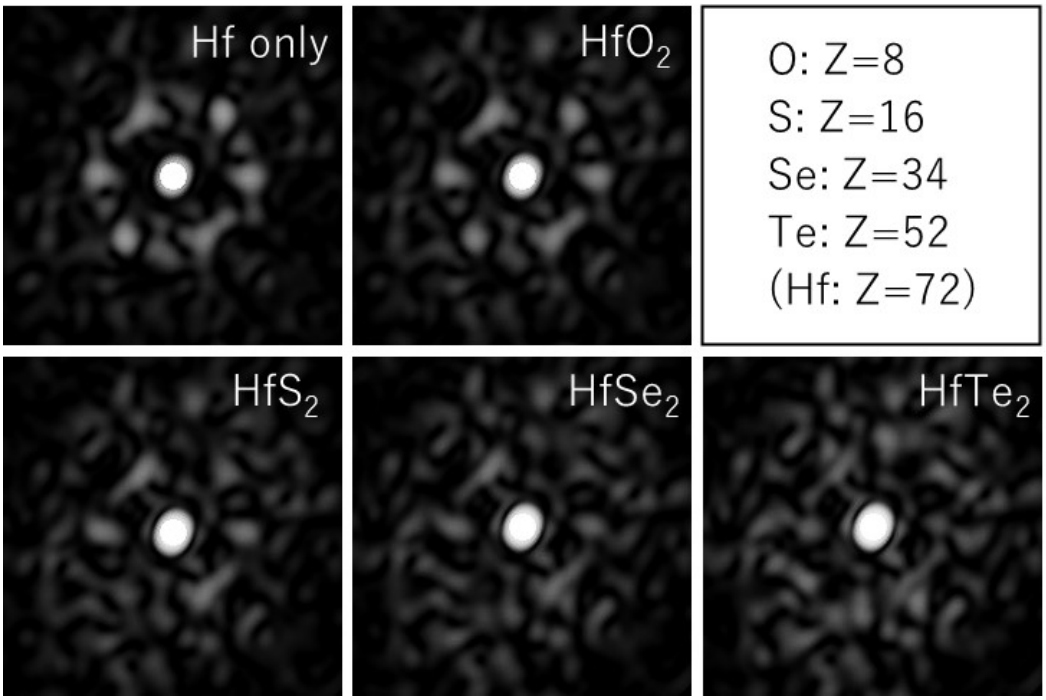

Supplementary Fig. 6　Calculated ABED patterns for the MRO model of HfO_2 with O sites substituted by various elements (vacancy (Hf only), O (Z=8), S (Z=16), Se (Z=34), Te (Z=52)). The ABED pattern of HfO_2 is almost unchanged compared to that of Hf only. However, when substituted with heavier elements (such as Se and Te), it exhibits a completely different ABED pattern. Since the atomic number of Hf is 72, the difference in atomic numbers between Hf and O contributes to seeing only the Hf sublattice.

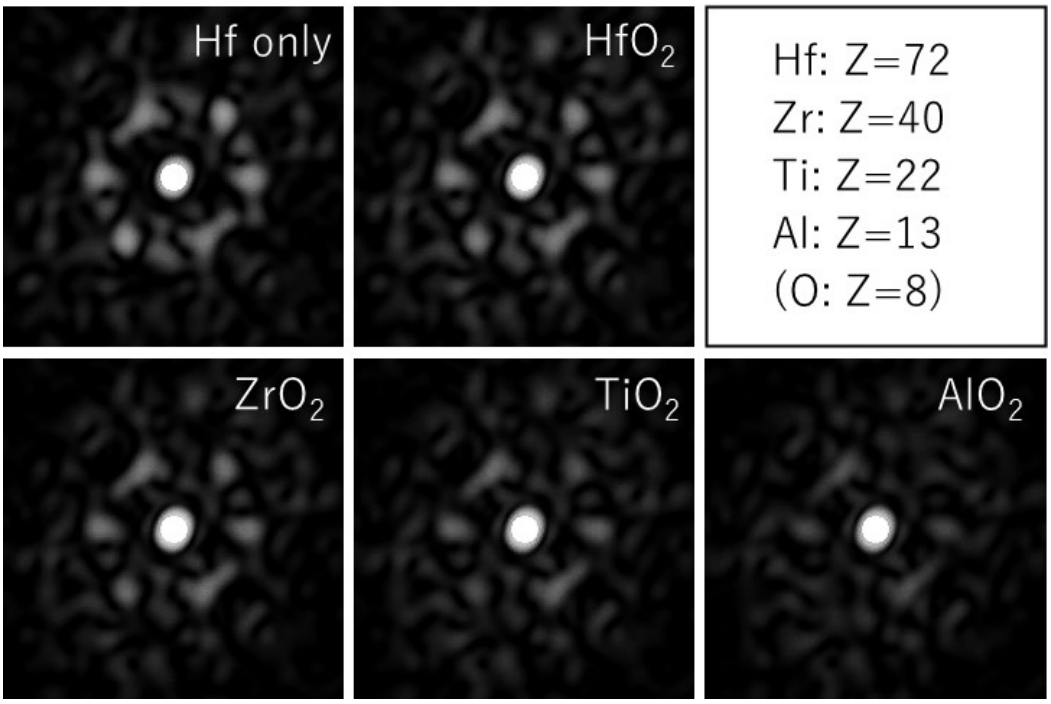

Supplementary Fig. 7　Calculated ABED patterns for the MRO model of HfO_2 with Hf sites substituted by various elements (Hf (Z=72), Zr (Z=40), Ti (Z=22), Al (Z=13)), together with the model including only Hf (the metal sublattice of HfO_2). The ABED pattern of HfO_2 is almost unchanged compared to that of Hf only. When Hf is substituted with lighter elements, the ABED pattern becomes significantly blurred. However, the ABED patterns of ZrO_2 and TiO_2 are still essentially the same as the ABED pattern of the metal sublattice. This result suggests that the ABED method allows us the observation of only the metal atoms in ZrO_2 and TiO_2, as well as in HfO_2.

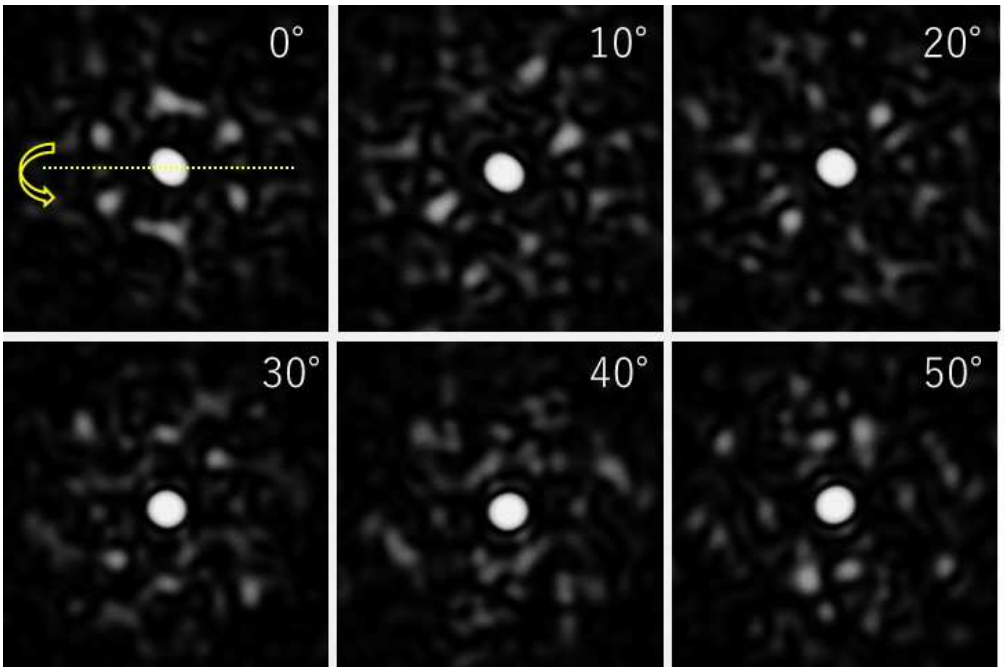

Supplementary Fig. 8　Simulated angstrom-beam electron diffraction (ABED) patterns obtained by rotating the medium-range order (MRO) structural model of amorphous HfO_2 derived from *ab initio* MD simulations around the axis shown in the figure. A pseudo-sixfold symmetric pattern appears only at the 0° orientation and is not found at other angles. This result demonstrates the strong orientation dependence of the diffraction pattern, indicating that the observed symmetry arises from a specific orientation of an anisotropic local structure. Although it would be preferable to experimentally obtain ABED patterns from different directions, this is technically unfeasible. In ABED experiments, tilting the sample inevitably shifts the illuminated region due to sample drift, making it difficult to maintain the same sub-nanometer region during rotation.

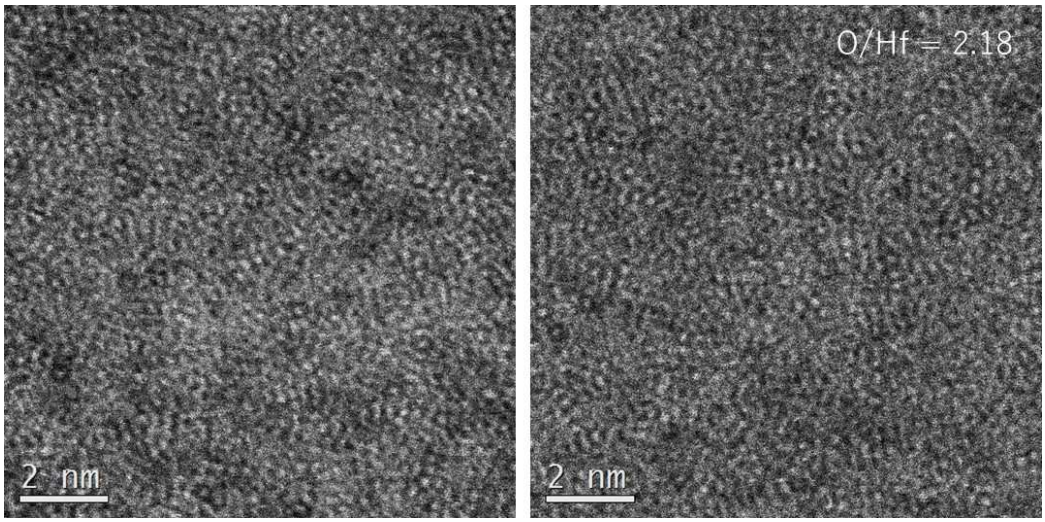

Supplementary Fig. 9 High-angle annular dark field scanning transmission electron microscope (HAADF-STEM) images obtained from amorphous HfO_2 thin film. The HAADF-STEM is roughly proportional to the square of the atomic number, basically reflecting the arrangement of Hf atoms, rather than O atoms. The absence of significant long-range structural order in the images indicates that the structure is amorphous. Energy-dispersive X-ray spectroscopy (EDS) analysis confirms an atomic ratio of O/Hf = 2.18, consistent with the expected stoichiometry of HfO_2.

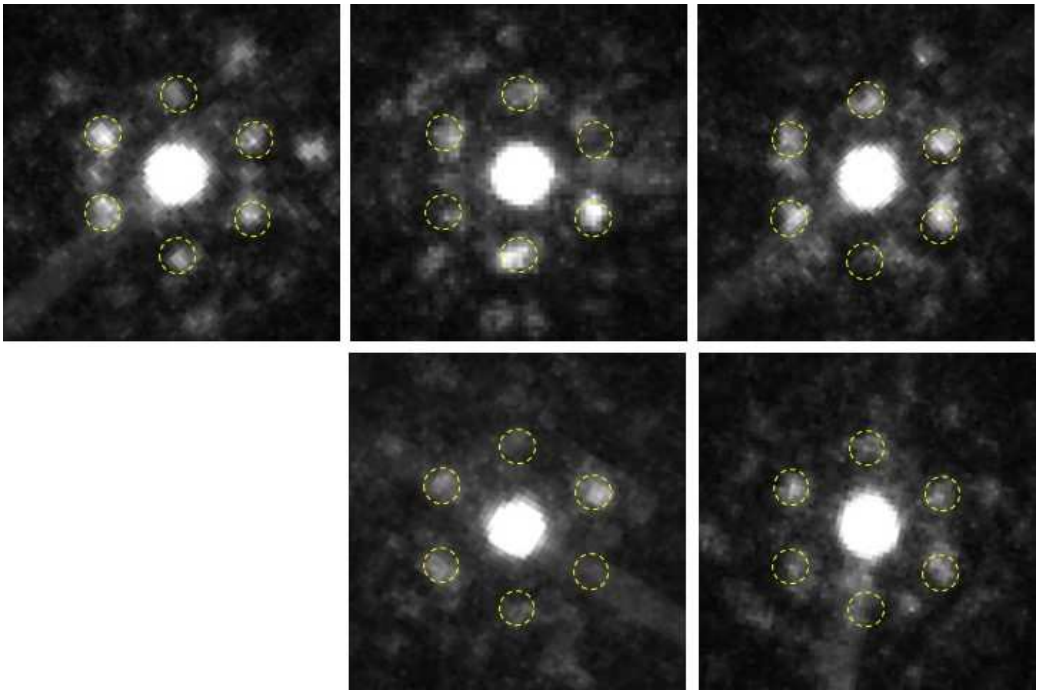

Supplementary Fig. 10 Experimental ABED patterns exhibiting a pseudo-sixfold symmetry obtained from amorphous HfO_2. Note that the upper left pattern is identical to the pattern of Fig. 2d. We assume that these patterns originate from MRO structures similar to the one shown in Fig. 2a Note that these highly symmetric ABED patterns are not frequently observed. However, this does not necessarily mean that such MRO structures are rare. As shown in Supplementary Fig. 8, the ABED pattern strongly depends on the orientation of the MRO structure, and therefore MRO structures rarely align with the orientation that produces a pseudo-sixfold pattern.

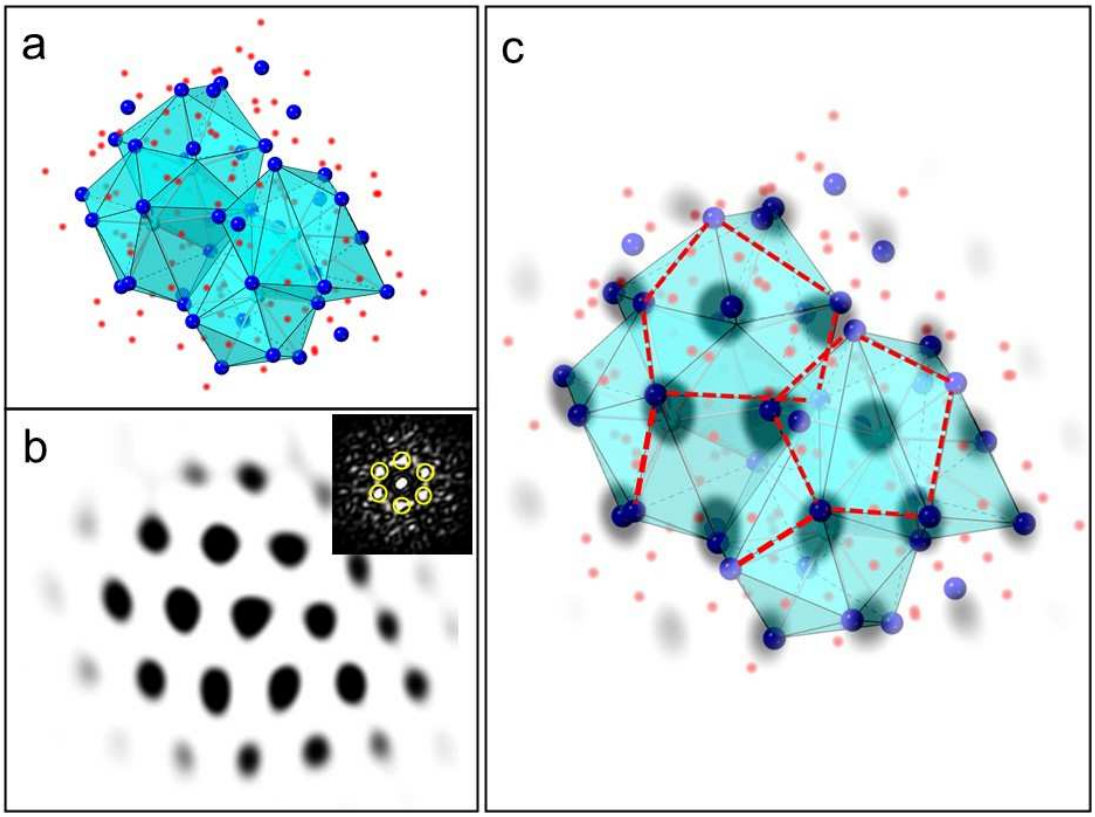

Supplementary Fig. 11 a, Medium-range order (MRO) structural region extracted from the amorphous HfO_2 model simulated using *ab initio* molecular dynamics. b, Fast Fourier transform (FFT) pattern obtained from the Hf atom arrangement in a, and inverse FFT (IFFT) image reconstructed using only the six strong spots marked in yellow forming a pseudo-triangular lattice. c, Superposition of the atomic configuration a and the IFFT image b. The red dotted lines highlight distorted pentagonal rings, which are approximately aligned with the lattice points of the pseudo-triangular lattice seen in the IFFT image. This suggests that the pseudo-sixfold symmetry arises from the spatial arrangement of interconnected fivefold structural units.

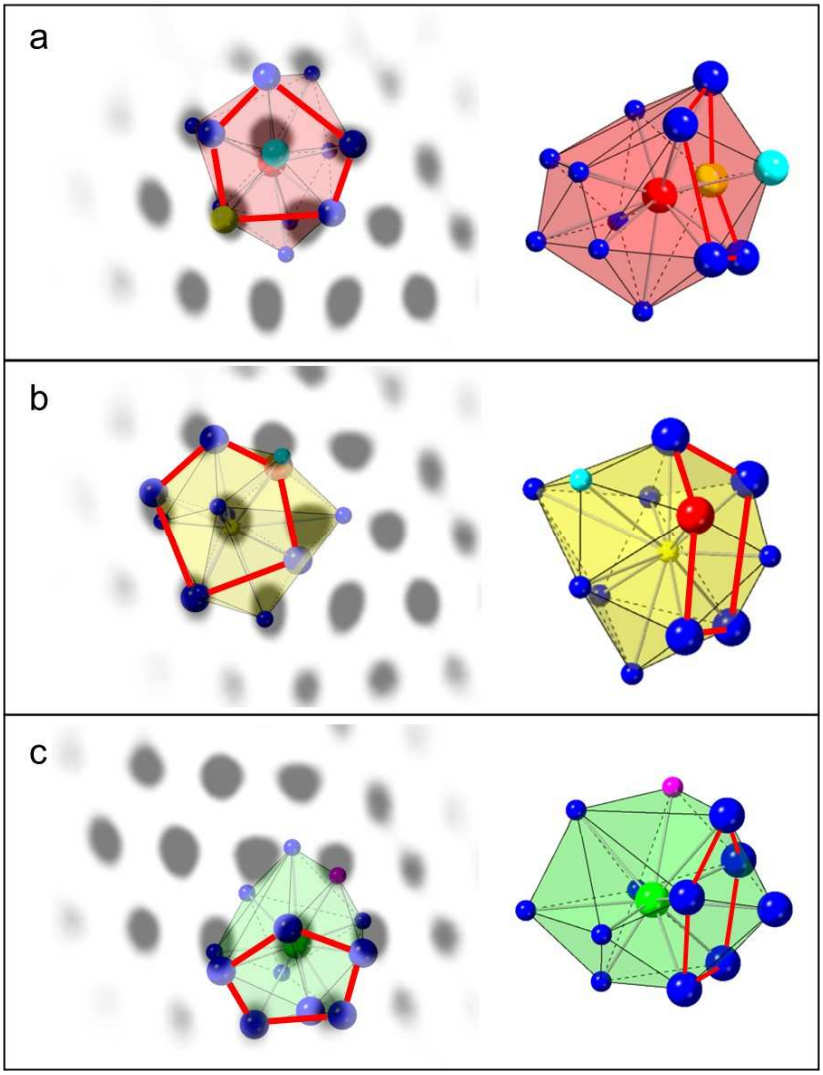

Supplementary Fig. 12 Three dodecahedral clusters in medium-range order (MRO) structural region extracted from the amorphous HfO_2 model simulated using *ab initio* molecular dynamics. The same clusters, viewed from different directions, are also shown on the right. Distorted pentagonal rings of pentagonal bipyramids are highlighted with bold red lines. The specific arrangement of these distorted pentagons within each cluster partially contributes to the formation of a pseudo-triangular lattice (IFFT image shown in Supplementary Fig. 11b), producing the pseudo-sixfold ABED pattern.

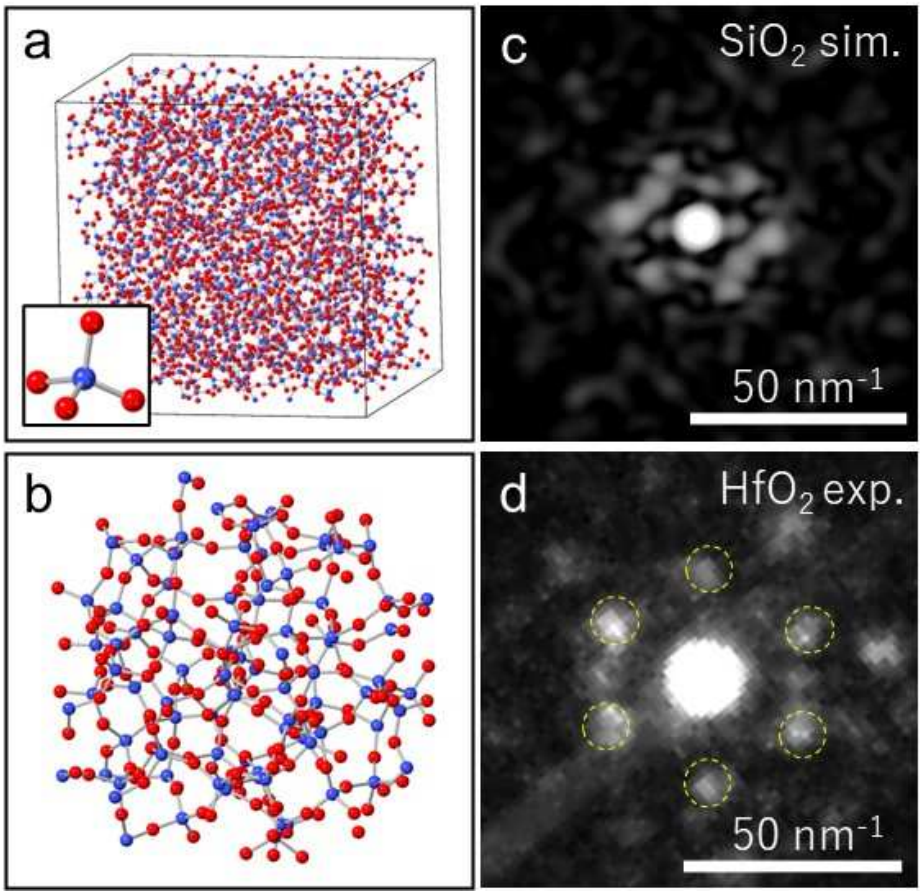

Supplementary Fig. 13 Atomic configuration and diffraction of amorphous SiO_2. a, Amorphous SiO_2 model simulated using molecular dynamics, together with a SiO_4 tetrahedral unit shown in the inset. b, MRO structure extracted from the model shown in a. c, Simulated ABED pattern of the MRO model shown in b. d, Experimental ABED pattern of amorphous HfO_2 as a reference. We found several diffraction spots from SiO_2 at lower scattering angles (Q ~ 1.5 Å^{-1}) than from amorphous HfO_2 (Q ~ 2.3 Å^{-1}). This means that the MRO in SiO_2 has a longer real-space periodicity (d ~ 4.2 Å) than that in HfO_2 (d ~ 2.7 Å), which in turn indicates that SiO_2 and HfO_2 have different structural motifs.

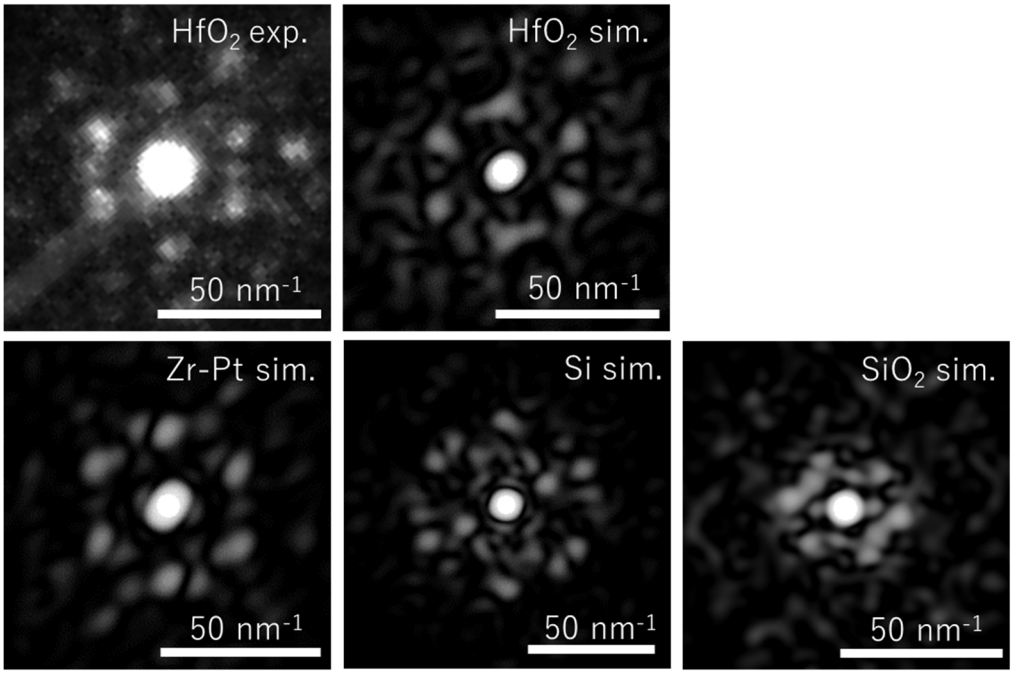

Supplementary Fig. 14　Comparison of pseudo-sixfold pattern in amorphous HfO_2, Zr-Pt metallic glass, amorphous Si, and amorphous SiO_2. Additionally, the experimental ABED pattern for amorphous HfO_2 is also shown.

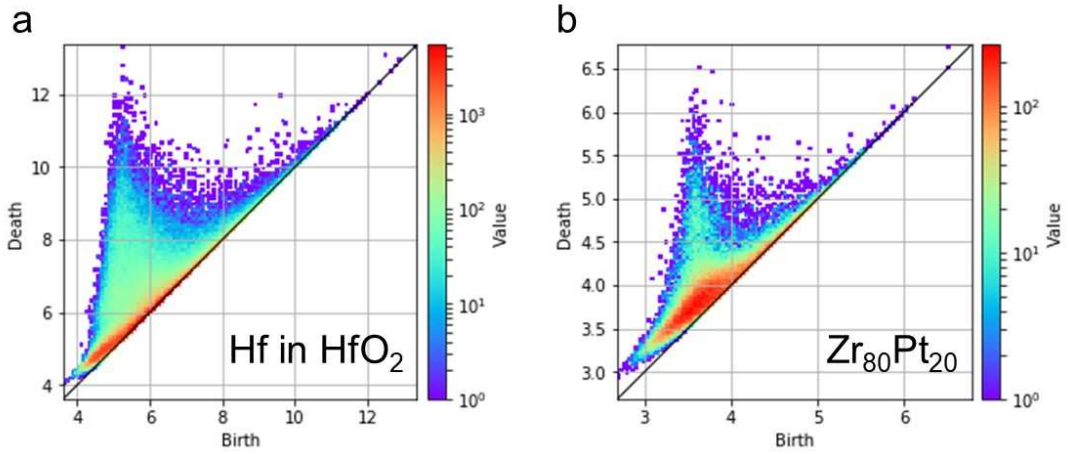

Supplementary Fig. 15 Second persistence diagrams (PD2) of Hf sublattice in amorphous HfO_2 (classical, 1.0×10^{13} K s^{-1}) (a), and of amorphous $Zr_{80}Pt_{20}$ (b).